J|A|C|S ARTICLES

Published on Web 04/21/2009

Role of Nucleobase Energetics and Nucleobase Interactions in Single-Stranded Peptide Nucleic Acid Charge Transfer

Amit Paul,[†] Silvia Bezer,[‡] Ravindra Venkatramani,[§] Laura Kocsis,[‡] Emil Wierzbinski,[†] Alexander Balaeff,[§] Shahar Keinan,[§] David N. Beratan,*[,§] Catalina Achim,*[,‡] and David H. Waldeck*[,†]

Department of Chemistry, University of Pittsburgh, Pittsburgh, Pennsylvania 15260, Department of Chemistry, Carnegie Mellon University, Pittsburgh, Pennsylvania 15213, and Departments of Chemistry and Biochemistry, Duke University, Durham, North Carolina 27708

Received January 2, 2009; E-mail: dave@pitt.edu (D.H.W.); achim@cmu.edu (C.A.); david.beratan@duke.edu (D.N.B.)

Abstract: Self-assembled monolayers of single-stranded (ss) peptide nucleic acids (PNAs) containing seven nucleotides (TTTXTTT), a C-terminus cysteine, and an N-terminus ferrocene redox group were formed on gold electrodes. The PNA monomer group (X) was selected to be either cytosine (C), thymine (T), adenine (A), guanine (G), or a methyl group (Bk). The charge transfer rate through the oligonucleotides was found to correlate with the oxidation potential of X. Kinetic measurements and computational studies of the ss-PNA fragments show that a nucleobase mediated charge transport mechanism in the deep tunneling superexchange regime can explain the observed dependence of the kinetics of charge transfer on the PNA sequence. Theoretical analysis suggests that the charge transport is dominantly hole-mediated and takes place through the filled bridge orbitals. The strongest contribution to conductance comes from the highest filled orbitals (HOMO, HOMO-1, and HOMO-2) of individual bases, with a rapid drop off in contributions from lower lying filled orbitals. Our studies further suggest that the linear correlation observed between the experimental charge transfer rates and the oxidation potential of base X arises from weak average interbase couplings and similar stacking geometries for the four TTTXTTT systems.

Introduction

Self-assembled monolayers (SAMs)[1,2] of nucleic acids are of interest in molecular electronics,[3] materials science,[4] molecular recognition,[5] biotechnology, and biosensor development.[6−8] A mechanistic understanding of charge transfer through such SAMs is important for the development of future applications. The past decade has seen considerable progress in understanding the charge transfer mechanism for DNA. The work of Sanche and co-workers[9] and Naaman[10] shows that low-energy electron capture can lead to damage and breaking of DNA strands. For hole transfer, guanine (G) bases act as a charge trap,[11] i.e., holes tend to localize on G, because of its lower oxidation potential relative to adenine (A), thymine (T), and cytosine (C). For short DNA duplexes, charge transfer between GC base pairs separated by AT base pairs is believed to follow a one-step superexchange mechanism,[12−18] whereas for long DNA duplexes, a multistep hopping mechanism is predominant.[11,19−23] Recent studies[24,25] indicate the possibility of mixed mechanisms, even at short distances.

[†] University of Pittsburgh.
[‡] Carnegie Mellon University.
[§] Duke University.

(1) Schwartz, D. K. *Annu. Rev. Phys. Chem.* **2001**, *52*, 107–137.
(2) Ulman, A. *Chem. Rev.* **1996**, *96*, 1533–1554.
(3) Jortner, J.; Ratner, M. A. *Molecular Electronics*; Blackwell: London, 1997.
(4) Kumar, A.; Biebuyck, H. A.; Whitesides, G. M. *Langmuir* **1994**, *10*, 1498–1511.
(5) Revell, D. J.; Knight, J. R.; Blyth, D. J.; Haines, A. H.; Russell, D. A. *Langmuir* **1998**, *14*, 4517–4524.
(6) Bain, C. D.; Evans, S. D. *Chem. Br.* **1995**, *31*, 46.
(7) Donhauser, Z. J.; Mantooth, B. A.; Kelly, K. F.; Bumm, L. A.; Monnell, J. D.; Stapleton, J. J.; Jr, D. W. P.; Rawlett, A. M.; Allara, D. L.; Tour, J. M.; Weiss, P. S. *Science* **2001**, *292*, 2303–2307.
(8) Prime, K. L.; Whitesides, G. M. *Science* **1991**, *252*, 1164–1167.
(9) Boudaiffa, B.; Cloutier, P.; Hunting, D.; Huels, M. A.; Sanche, L. *Science* **2000**, *287*, 1658–1660.
(10) Ray, S. G.; Daube, S. S.; Naaman, R. *Proc. Natl. Acad. Sci.* **2005**, *102*, 15–19.
(11) Schuster, G. B. *Long-Range Charge Transfer in DNA I. in Top. Curr. Chem. Vols 236 and 237*; Springer: New York, 2004.
(12) Tong, G. S. M.; Kurnikov, I., V.; Beratan, D. N. *J. Phys. Chem. B* **2002**, *106*, 2381–2392.
(13) Joachim, C.; Ratner, M. A. *Nanotechnology* **2004**, *15*, 1065.
(14) Magoga, M.; Joachim, C. *Phys. Rev. B* **1997**, *56*, 4722.
(15) Priyadarshy, S.; Risser, S. M.; Beratan, D. N. *J. Phys. Chem.* **1996**, *100*, 17678–17682.
(16) Ratner, M. A. *J. Phys. Chem.* **1990**, *94*, 4877–4883.
(17) Reimers, J. R.; Hush, N. S. *J. Photochem. Photobiol. A* **1994**, *82*, 31–46.
(18) Remacle, F.; Levine, R. D. *J. Phys. Chem. B* **2001**, *105*, 2153–2162.
(19) Berlin, Y. A.; Burin, A. L.; Ratner, M. A. *Chem. Phys.* **2002**, *275*, 61–74.
(20) Berlin, Y. A.; Hutchison, G. R.; Rempala, P.; Ratner, M. A.; Michl, J. *J. Phys. Chem. A* **2003**, *107*, 3970–3980.
(21) Giese, B. *Annu. Rev. Biochem.* **2002**, *71*, 51–70.
(22) Jortner, J.; Bixon, M.; Langenbacher, T.; Michel-Beyerle, M. E. *Proc. Natl. Acad. Sci.* **1998**, *95*, 12759.
(23) Li, X. Q.; Zhang, H.; Yan, Y. *J. Phys. Chem. A* **2001**, *105*, 9563–9567.
(24) Hatcher, E.; Balaeff, A.; Keinan, S.; Venkatramani, R.; Beratan, D. N. *J. Am. Chem. Soc.* **2008**, *130*, 11752–11761.
(25) Valis, L.; Wang, Q.; Raytchev, M.; Buchvarov, I.; Wagenknecht, H.-A.; Fiebig, T. *Proc. Natl. Acad. Sci.* **2006**, *103*, 10192–10195.

 10.1021/ja9000163 CCC: $40.75

Charge transfer for DNA in solution has been studied extensively, but only a few studies have addressed DNA charge transfer mechanisms in SAMs, possibly because of the difficulty of creating DNA SAMs on a metal surface.[26−28] Some studies have explored the conductivity through DNA, intimately related to charge transfer, by break junction methods,[29] scanning tunneling microscopy techniques,[30,31] and current sensing atomic force microscopy.[32] These studies demonstrated that the conductivity of the DNA molecules can be significantly enhanced by the presence of G bases. The challenge of creating monolayers of well-characterized structures is particularly large for single-stranded (ss)-DNA. Hartwich et al.[33] studied charge transfer for mixed monolayers of a ss 12-mer DNA with a pyrrolo-quinoline−quinone redox probe attached to DNA through a spacer, and linked the molecule to a Au(111) surface through an ethane-thiol linker. The CT rate constant was too slow to be measured by cyclic voltammetry at a scan rate of >10 mV s^{-1}. Chahma et al.[34] reported a CT rate constant of 12 s^{-1} for a 20 base ss-DNA monolayer, which was only 10 times slower than the rate in the corresponding double-stranded (ds)-DNA monolayer. In contrast, Anne et al. reported charge transfer rate constants of 2×10^4 to 4×10^4 s^{-1} for low coverages of ss 20-mer DNA,[35,36] for which the redox reporter (ferrocene) is believed to be localized near the metal surface. The limited success of earlier studies and the challenge of making compact films with charged DNA oligomers motivated us to seek an alternative approach to explore charge transfer through nucleobase stacks in organized monolayers.

In contrast to the negatively charged and chiral DNA backbone, the backbone of peptide nucleic acid (PNA) based on aminoethylglycine is neutral and achiral (Figure 1).[37,38] Therefore, PNA is a good candidate for self-assembly on surfaces. PNA forms duplexes with itself and with DNA by Watson−Crick base pairing.[37−42] PNA·PNA duplexes adopt a so-called P-type helical structure, which has a pitch of 18 bases/turn, a diameter of 28 Å, and a 3.2−3.4 Å rise/base pair.[39−42] Although the PNA backbone is achiral, a preferred handedness can be induced in PNA duplexes by covalently attaching a chiral amino acid to the C-terminus of the PNA oligomers.[43]

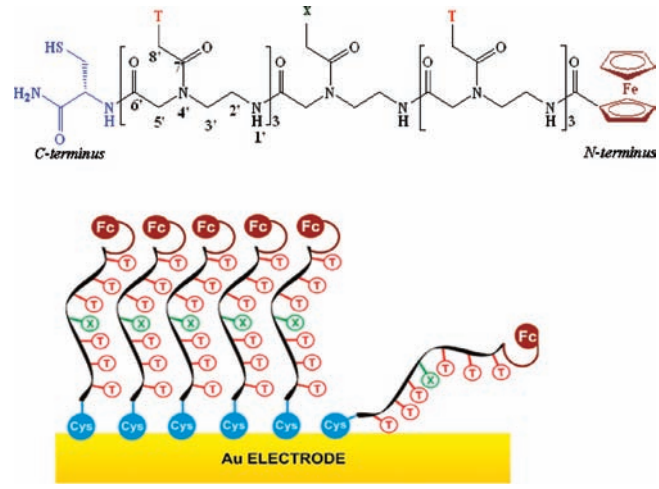

Figure 1. (Top) Chemical structure of ss-PNA with C-terminus cysteine and N-terminus ferrocene. (Bottom) ss-PNA molecules self-assembled on a gold surface. The blue circle represents cysteine; the black curve represents the PNA backbone. The nucleobases are represented by open circles. The variable base is represented as an X. X is methyl group (Bk), C, T, A or G. The brown circle represents ferrocene.

Recently, we reported the results of a study of charge transfer through SAMs composed of short ss-PNA containing several thymine nucleobases.[44] The charge-transfer mechanism was found to be hole-mediated superexchange with an exponential decay constant (β) of 0.86 $Å^{-1}$. This β value is similar to that for alkanethiols[45−49] and peptides[50,51] and is consistent with expectations for base-mediated hole transport in the deep tunneling regime.[15] The study reported here probes the role of nucleobases in mediating the tunneling by studying five different 7-mer ss-PNAs (Figure 1). PNA with a ferrocene redox probe covalently attached at the N-terminus was immobilized on a gold surface through a cysteine group at the C-terminus (Figure 1). The first three and last three nucleotides of each strand were T bases, and the fourth (central) monomer was either G, A, C, T, or a methyl group (Bk). The charge transfer rate constant in the PNA SAMs, measured by cyclic voltammetry, changed by more than 15-fold as the central PNA base was varied. This result demonstrates that the nucleobases play a significant role in mediating the charge tunneling through PNA.

(26) Casero, E.; Darder, M.; Diaz, D. J.; Pariente, F.; Martin-Gago, J. A.; Abruna, H.; Lorenzo, E. *Langmuir* **2003**, *19*, 6230–6235.
(27) Herne, T. M.; Tarlov, M. J. *J. Am. Chem. Soc.* **1997**, *119*, 8916–8920.
(28) Zhang, R. Y.; Pang, D. W.; Zhang, Z. L.; Yan, J. W.; Yao, J. L.; Tian, Z. Q.; Mao, B. W.; Sun, S. G. *J. Phys. Chem. B* **2002**, *106*, 11233–11239.
(29) (a) Xu, B.; Zhang, P.; Li, X.; Tao, N. *Nano. Lett.* **2004**, *4*, 1105–1108. (b) Hihath, J.; Xu, B.; Zhang, P.; Tao, N. *Proc. Natl. Acad. Sci.* **2005**, *102*, 16979–16983.
(30) van Zalinge, H.; Schiffrin, D. J.; Bates, A. D.; Haiss, W.; Ulstrup, J.; Nichols, R. *J. ChemPhysChem* **2006**, *7*, 94–98.
(31) Wierzbinski, E.; Arndt, J.; Hammond, W.; Slowinski, K. *Langmuir* **2006**, *22*, 2426–2429.
(32) (a) Nogues, C.; Cohen, S. R.; Daube, S.; Apter, N.; Naaman, R. *J. Phys. Chem. B* **2006**, *110*, 8910–8913. (b) Nogues, C.; Cohen, S. R.; Daube, S. S.; Naaman, R. *Phys. Chem. Chem. Phys.* **2004**, *6*, 4459–4466.
(33) Hartwich, G.; Caruana, D. J.; de Lumley-Woodyear, T.; Wu, Y.; Campbell, C. N.; Heller, A. *J. Am. Chem. Soc.* **1999**, *121*, 10803–10812.
(34) Chahma, M.; Lee, J. S.; Kraatz, H.-B. *J. Electroanal. Chem.* **2004**, *567*, 283–287.
(35) Anne, A.; Demaille, C. *J. Am. Chem. Soc.* **2006**, *128*, 542–557.
(36) Anne, A. s.; Demaille, C. *J. Am. Chem. Soc.* **2008**, *130*, 9812–9823.
(37) Egholm, M.; Buchardt, O.; Christensen, L.; Behrens, C.; Freier, S. M.; Driver, D. A.; Berg, R. H.; Kim, S. K.; Norden, B.; Nielsen, P. E. *Nature (London)* **1993**, *365*, 566–568.
(38) Egholm, M.; Nielsen, P. E.; Buchardt, O.; Berg, R. H. *J. Am. Chem. Soc.* **1992**, *114*, 9677–9678.
(39) He, W.; Hatcher, E.; Balaeff, A.; Beratan, D. N.; Gil, R. R.; Madrid, M.; Achim, C. *J. Am. Chem. Soc.* **2008**, *130*, 13264–13273.
(40) Petersson, B.; Nielsen, B. B.; Rasmussen, H.; Larsen, I. K.; Gajhede, M.; Nielsen, P. E.; Kastrup, J. S. *J. Am. Chem. Soc.* **2005**, *127*, 1424–1430.
(41) Rasmussen, H.; Kastrup, J. S.; Nielsen, J. N.; Nielsen, J. M.; Nielsen, P. E. *Nat. Struct. Biol.* **1997**, *4*, 98–101.
(42) Rasmussen, H.; Liljefors, T.; Petersson, B.; Nielsen, P. E.; Kastrup, J. S. *J.Biomol. Struct. Dyn.* **2004**, *21*, 495–502.
(43) Wittung, P.; Eriksson, M.; Lyng, R.; Nielsen, P. E.; Norden, B. *J. Am. Chem. Soc.* **1995**, *117*, 10167–10173.
(44) Paul, A.; Watson, R. M.; Lund, P.; Xing, Y.; Burke, K.; He, Y.; Borguet, E.; Achim, C.; Waldeck, D. H. *J. Phys. Chem. C* **2008**, *112*, 7233–7240.
(45) Carter, M. T.; Rowe, G. K.; Richardson, J. N.; Tender, L. M.; Terrill, R. H.; Murray, R. W. *J. Am. Chem. Soc.* **1995**, *117*, 2896–2899.
(46) Slowinski, K.; Chamberlain, R. V.; Miller, C. J.; Majda, M. *J. Am. Chem. Soc.* **1997**, *119*, 11910–11919.
(47) Smalley, J. F.; Feldberg, S. W.; Chidsey, C. E. D.; Linford, M. R.; Newton, M. D.; Liu, Y.-P. *J. Phys. Chem.* **1995**, *99*, 13141–13149.
(48) Sumner, J. J.; Weber, K. S.; Hockett, L. A.; Creager, S. E. *J. Phys. Chem. B* **2000**, *104*, 7449–7454.
(49) Weber, K.; Hockett, L.; Creager, S. *J. Phys. Chem. B* **1997**, *101*, 8286–8291.
(50) Sek, S.; Sepiol, A.; Tolak, A.; Misicka, A.; Bilewicz, R. *J. Phys. Chem. B* **2004**, *108*, 8102–8105.
(51) Tao, N. *J. Mater. Chem.* **2005**, *15*, 3260–3263.

Theoretical calculations of charge transport through ss 7-mer PNAs T3−X−T3 (X = G, A, C, T) were performed using the nonequilibrium Green's function (NEGF) method on the ensemble of structures obtained from constrained molecular dynamics (MD) simulations that sampled the base geometries and stacking interactions for each T3−X−T3 PNA. The ensemble-averaged conductance values (calculated near zero bias) correlate well with the experimental charge-transfer rates. These studies also show that the observed differences in experimental rates for the PNA SAMs can be explained in terms of charge tunneling mediated by the nucleobases.

Experimental and Computational Details

Synthesis of *N*-(2-Boc-aminoethyl)-*N*-(methyl)-glycine. Boc-Aeg-O^{t}Bu (3 g, 10.9 mmol) was added to a stirring solution of 1-ethyl-3-(3-dimethylaminopropyl)carbodiimide hydrochloride) (EDC) (2.4 g, 12.5 mmol), glacial acetic acid (0.8 mL, 12.5 mmol), *O*-benzotriazole-*N*,*N*,*N*′,*N*′-tetramethyl-uronium-hexafluorophosphate (HBTU) (4.8 g, 12.5 mmol), and *N*,*N*-diisopropylethylamine (DIPEA) (4.1 mL, 22.5 mmol) in 250 mL CH_2Cl_2. The solution was stirred for 24 h, and then washed with H_2O (5 × 100 mL). The organic part was dried with Na_2SO_4. The oil obtained after evaporation of CH_2Cl_2 was purified by silica gel chromatography (Hex/EtOAc = 1:1). The solvent was then evaporated to afford 2.2 g (64%) of the ^{t}Butyl ester of *N*-(2-Boc-aminoethyl)-*N*-(methyl)-glycine as a white solid. ^{1}H NMR (300 MHz, $CDCl_3$) 1.5 (18H, 2s, 2*t*-butyl-CH_3), 2−2.2 (3H, major+minor(s), CH_3), 3.2 (2H, m, CH_2), 3.4−3.5 (m, CH_2), 3.9−4.0 (2H, major+minor(s), CH_2), 5.5 (1H, s, N*H*). 2 mL of 25 M NaOH solution was added dropwise to a solution of ^{t}Butyl ester of *N*-(2-Boc-aminoethyl)-*N*-(methyl)-glycine (2.2 g, 7 mmol) in 84 mL of ethanol/water 1:2 (v/v) at room temperature. After the mixture was stirred for 24 h, the pH was adjusted to 3 using HCl. After extraction with EtOAc (5 × 100 mL) and drying under vacuum, *N*-(2-Boc-aminoethyl)-*N*-(methyl)-glycine has been obtained as a yellow oil (1.5 g, 83%). ^{1}H NMR (300 MHz, $CDCl_3$): 1.5 (9Hs, *t*-butyl-CH_3), 2−2.2 (3H, major+minor(s), CH_3), 3.2 (2H, m, CH_2), 3.4−3.5 (2H, m, CH_2), 3.9−4.0 (2H, major+minor(s), CH_2), 5.5 (1H, s, N*H*). ESI-MS calcd for [M + Na^+] 283.28; found 282.98.

PNA Synthesis. PNA oligomers were synthesized using solid phase peptide synthesis methods with a Boc protection strategy.[52−54] MBHA resin (Peptides International, Louisville, KY) with a loading of 0.18 mequiv/g was down-loaded[54] using Boc-L-Cys-(4-MeOBzl)-OH (NovaBiochem/Merck Biosciences, Switzerland) to an estimated loading of 0.04−0.06 mequiv/g. Thereafter depending on sequence, Boc-T-OH/ Boc-(A-Z)-OH/ Boc-(G-Z)-OH/ Boc-(C-Z)-OH (Applied Biosystems, Foster City, CA) or *N*-(2-Boc-aminoethyl)-*N*-(methyl)-glycine were coupled using 1*H*-Benzotriazolium 1-[*bis*(dimethylamino) methylene]-5chloro-hexafluorophosphate (1),3-oxide (HCTU) (Peptides International) as a coupling agent. Finally, ferrocene carboxylic acid (Aldrich) was coupled to the N-terminus. This coupling was repeated twice to increase the yield of ferrocene-conjugated PNA. Oligomers were cleaved from the resin using trifluoroacetic acid (TFA) and trifluoromethanesulfonic acid (TFMSA), precipitated in ethyl ether, and dried under nitrogen. The solid products were dissolved in 15% acetonitrile aqueous solution and purified by reverse-phase HPLC using a solvent gradient, from 15% to 35% acetonitrile in water over 40 min on a Waters Delta 600 pump with a 2996 photodiode-array detector (Milford, MA). PNA oligomers were characterized by MALDI-TOF mass spectrometry on an Applied Biosystems Voyager-DE STR Workstation.

PNA solutions were prepared in deionized water, and the PNA concentrations were determined by UV−vis spectrophotometry assuming ε_{260} = 8600, 6600, 13 700, and 11 700 cm^{-1} M^{-1} for each T, C, A, and G monomer, respectively.[54] PNA solutions for electrode incubation were typically 20 μM ss-PNA in 1:1 (v/v) acetonitrile/10 mM pH 7.0 sodium phosphate buffer.

Electrode Preparation. A gold wire (0.5 mm diameter, 99.999%, Alfa Aesar, MA) was cleaned by reflux in nitric acid (70%) at 130 °C for 2 h and then washed with deionized water (>18 MΩ·cm). The wire was sealed in a soft-glass capillary tube with the tip exposed. The tip of the gold wire was heated to form a ball. The gold ball was reheated in a flame until glowing, then slowly cooled, and finally quenched in deionized water (>18 MΩ·cm). This annealing process was repeated more than 15 times until a smooth ball electrode was obtained. The area of the electrode was determined electrochemically[55] and found to be typically ∼0.1 cm^2.

SAM Preparation. SAMs were prepared by incubating gold ball electrodes in 1 mL of a 20 μM ss-PNA solution for 28 h at 40 °C. After incubation, the gold electrodes were washed with deionized water (>18 MΩ·cm) and directly used in the electrochemical studies.

Electrochemical Measurements. Cyclic voltammetry was carried out on a CH Instrument Electrochemical Analyzer 618B (Austin, TX). The three-electrode electrochemical cell consisted of an Ag/AgCl (3 M KCl) reference electrode, a platinum wire as a counter electrode, and a SAM-coated gold ball electrode as the working electrode. All experiments were performed in 1 M $NaClO_4$ (pH 7−8) aqueous electrolyte solution at room temperature. The uncompensated solution resistance was measured by AC impedance and found to be less than 5 Ω, so that the *iR* drop was not important for these measurements. The coverage of the PNA−ferrocene SAM was calculated by integrating the charge under the voltammetric peaks.

Ellipsometry. Film thickness was measured by ellipsometry.[56,57] The molecules were self-assembled to form a monolayer film on evaporated gold slides (EMF Corp, Ithaca, NY). The Au slides were 0.7 in. × 0.3 in. × 0.062 in. in size and consisted of about 100 nm Au over a 50 nm thick Ti binder layer on float glass. The gold slides were cleaned by immersion in "piranha" solution (1:3 H_2O_2 and 98% H_2SO_4) (**Caution:** *The piranha solution is a very strong oxidizing agent and extremely dangerous. Eye protection and gloves should be used during handling!*) for 2 min, then rinsed with a large amount of deionized water, followed by ethanol. They were, subsequently dried under nitrogen. The Au slides were incubated in 1.0 mL of a 20 μM ss PNA solution for 28 h at 40 °C. After incubation, these SAM-coated gold slides were rinsed vigorously with ethanol and water and dried under nitrogen. The thickness was measured by a Gaertner L-117 Null ellipsometer.

Molecular Dynamics Simulations. Structures of the four ss-PNA sequences T3−X−T3 (X = G, A, C, T) were constructed by extending/mutating the PNA hexamer structure of Rasmussen and Kastrup[41] (PDB code 1PUP), as described earlier.[24] The structures were solvated in a 70 Å × 70 Å × 70 Å box of TIP3 water, and simulated with NAMD[58] using the AMBER[59] force field modified for PNA.[39] The simulations employed the NPT ensemble, periodic boundary conditions, and P3ME full electrostatics. The bond lengths between the hydrogens and the heavy atoms were allowed to fluctuate. To ensure the numerical stability of the MD simulation with unrestrained hydrogens, a MD time step of 0.5 fs was used.

(52) Anderson, G. W.; McGregor, A. C. *J. Am. Chem. Soc.* **1957**, *79*, 6180–6183.
(53) McKay, F. C.; Albertson, N. F. *J. Am. Chem. Soc.* **1957**, *79*, 4686–4690.
(54) Nielsen, P. E. *Peptide Nucleic Acids: Protocols and Applications*; Horizon Bioscience: Wymondham, UK, 2004.
(55) Sawyer, D. T.; Sobkowiak, A.; Roberts, J. L. *Experimental Electrochemistry for Chemists*; Wiley: New York, 1995.
(56) Azzam, R. M. A.; Bashara, N. M. *Ellipsometry and Polarized Light*; North-Holland Publishing Co.: Amsterdam, 1977.
(57) Tompkins, H. G. *A User's Guide to Ellipsometry*; Academic Press, Inc.: Boston, 1993.
(58) Phillips, J. C.; Braun, R.; Wang, W.; Gumbart, J.; Tajkhorshid, E.; Villa, E.; Chipot, C.; Skeel, R. D.; Kalé, L.; Schulten, K. *J. Comput. Chem.* **2005**, *26*, 1781–1802.
(59) Case, D. A.; Walker, R. C. *Amber, 9*: University of California: San Francisco, 2006.

The simulations consisted of 0.5 ns-long water equilibration around frozen PNA, a gradual release of the PNA during the next 0.5 ns, and finally a 0.5 ns-long production stage. Five hundred snapshots were saved during the production stage at every 1 ps for electronic structure analysis.

The initial MD simulations showed that the extremely flexible PNA backbone produced a variety of bent conformations that could not be adequately sampled on the MD time scales accessed here; for a comparison with earlier PNA simulations by others,[60] see the Supporting Information. Therefore, the PNA was restrained near its initial structure by harmonically constraining the positions of the C7′ and N4′ atoms that tether each nucleobase to the backbone (cf. Figure 1). Such restraints effectively freeze the global conformation of the PNA backbone to that found in the 1PUP structure, while providing the nucleobases with rotational mobility around the unrestrained C7′−C8′ and C8′−N1/N9 bonds. Presumably, the restrained conformations of the PNA mimic the conformations that the molecules adopt in the PNA films. For the surface coverages used here, the molecules are expected to be "standing up" on the metal surface. Nevertheless, it is possible that these constrained conformations introduce artifacts into the distributions of calculated properties (e.g., asymmetries introduced in calculated charge transport properties by enforcing a larger overlap between bases 3 and 4 compared to that between bases 4 and 5 present in the 1PUP structures—cf. Figure 7). Despite these limitations, we expect the structures to capture relative trends in charge transport across the four different PNA systems. As shown in subsequent sections, good correlations between calculated and experimental trends are observed.

Electronic Structure Analysis. For each MD snapshot of a T3−X−T3 system (X = G, A, C, T), the atomic coordinates of the three central bases (T−X−T, referred to hereafter as the core unit) were extracted, and the dangling bonds were capped with hydrogens using VMD.[61] Since mutation of a single base will induce changes primarily in both energies and nearest neighbor couplings, this core segment is expected to capture essential differences in charge transfer rates among the four T3−X−T3 systems. The higher order couplings are neglected because they are at least an order of magnitude weaker than the nearest neighbor couplings.[62,63] The electronic structure of the core unit was analyzed using single point self-consistent field calculations with the INDO/s method implemented in the CNDO program.[64] This approach is widely used to compute donor−acceptor couplings in DNA.[63] The calculated molecular orbitals (MOs) and their energies were used as the input for the NEGF method to calculate transport properties.

The semiempirical INDO/s approach[65] provides a useful balance between cost and performance,[66] especially for electronic structures with a strong propensity for CT, where density functional theory methods may fail.[67] The application of various quantum-mechanical methods to compute the donor and acceptor coupling in nucleic acids has been reviewed,[68] and it was found that the INDO/s results agree well with higher-level ab initio calculation such as CASPT2 and CASSCF. Further, INDO/s calculations are at least two orders of magnitude faster than the higher-level calculations, making them indispensable for dealing with the thousands of MD snapshots generated in this present study.

NEGF Method. The NEGF formalism[69] describes transport through a molecule in contact with electrodes. The Green's function, G, is

$$G(\varepsilon) = \frac{1}{(\varepsilon \mathbf{I} - \mathbf{H} - \mathbf{\Sigma}_L - \mathbf{\Sigma}_R)} \quad (1)$$

Here $\mathbf{H}$ is the Fock matrix of the molecule and ε is the energy variable. The self-energy matrix, $\mathbf{\Sigma}$, describes molecular eigenstate broadening and shifts induced by coupling to left (L) and right (R) electrodes, which are not explicitly modeled. The transmission is

$$T(\varepsilon) = Tr[\mathbf{\Gamma}_L \mathbf{G} \mathbf{\Gamma}_R \mathbf{G}^+] \quad (2)$$

where the broadening matrix $\mathbf{\Gamma} = i\,[\mathbf{\Sigma} - \mathbf{\Sigma}^+]$ is related to the imaginary part of the self-energy matrix $\mathbf{\Sigma}$. The values of the broadening matrix are chosen to be at least one order of magnitude smaller than the difference in energies (diagonal terms) of the Fock matrix elements expressed in the basis of atomic orbitals. This places us in the weak electrode−molecule coupling limit where the coupling with the electrode does not change the molecular eigenstates/eigenenergies significantly. We assume further that only the carbon and nitrogen atoms of the nucleobase rings are coupled to the electrode since charge transport in DNA is thought to be π mediated and these atoms constitute the centers of the atomic π orbitals.[11] The broadening matrix element values were taken to be $\Gamma_{ii} = 0.1$ eV for all thymine carbon and nitrogen atoms, $\Gamma_{ii} = 0$ for all other atoms, and $\Gamma_{ij} = 0$ for $i \neq j$ (i and j are atomic orbital indices). The effects of the thymine bases outside the core unit and of the cysteine linker are included via the effective coupling, as represented by the broadening matrix. This choice of weak electrode-molecule perturbation allows us to link the calculated conductance, which is a steady-state property, to the experimental CT rate constant.[70]

Current as a function of applied bias is related to the transmission coefficient through the Landauer expression:

$$I(V) = \frac{q}{h} \int T(\varepsilon)[f_L(\varepsilon) - f_R(\varepsilon)]\, d\varepsilon \quad (3)$$

where f_L and f_R are Fermi functions defining the electron occupancies for the left and right contacts. The current for a small applied potential bias (up to 100 mV) was calculated, assuming a fixed value for the metal Fermi energy, (ε_F is taken to lie 0.8 eV above the HOMO of the TXT core). This value of ε_F is given by the oxidation potential of the ferrocene which is 0.8 eV below that of guanine, as reported in the experiments of Seidel et al.[71] Because the dominating contribution to the current (in eq 3) comes from the transmission near the Fermi energy, we can write $I(V) \approx (q/h) \cdot T(\varepsilon = \varepsilon_F)$. By expressing $\mathbf{\Gamma}$ and $\mathbf{G}$ in the basis of MOs in eq 2, we see that the transmission (and the current) may be decomposed into contributions arising from specific orbitals: $T(\varepsilon = \varepsilon_F) = \sum_m SF_m$. The scoring factor SF_m gives the contribution of orbital m to the current and is

$$SF_m = \sum_n \frac{\Gamma^L_{mn}\Gamma^R_{nm}}{(\varepsilon_F - \varepsilon_m)(\varepsilon_F - \varepsilon_n)} \quad (4)$$

where the index n sums over all MOs. In eq 4, we use the approximation that $\varepsilon_F - \varepsilon_m + 0.5i\Gamma_{mm} \approx \varepsilon_F - \varepsilon_m$. The terms with $m = n$ represent a pure contribution from orbital m with matrix elements Γ^L_{mm} and Γ^R_{mm} representing its broadening, due to interactions with the left and right electrodes, respectively. The pure contributions are always positive. The terms with $m \neq n$, represent

(60) Sen, S.; Nilsson, L. *J. Am. Chem. Soc.* **2001**, *123*, 7414–7422.
(61) Humphrey, W.; Dalke, A.; Schulten, K. *J. Molecular Graphics* **1996**, *14*, 33–38.
(62) Mehrez, H.; Anantram, M. P. *Phys. Rev. B* **2005**, *71*, 115405–5.
(63) Rösch, N.; Voityuk, A. A. In *Long-Range Charge Transfer in DNA II*; Springer: New York, 2004; pp 37−72.
(64) Zeng, J.; Hush, N. S.; Reimers, J. R. *J. Am. Chem. Soc.* **1996**, *118*, 2059–2068.
(65) Ridley, J.; Zerner, M. *Theor. Chim. Acta* **1973**, *32*, 111–134.
(66) Thiel, W. Semiempirical quantum-chemical methods in computational chemistry. In *Theory and Applications of Computational Chemistry: The First 40 Years*; Dykstra, C. E., Kim, K. S., Frenking, G., Scuseria, G. E., Eds.; Elsevier: Amsterdam, 2005; pp 559−580.
(67) Hutchison, G. R.; Ratner, M. A.; Marks, T. J. *J. Phys. Chem. A* **2002**, *106*, 10596–10605.
(68) Rosch, N.; Voityuk, A. A. *Top. Curr. Chem.* **2004**, *237*, 37–72.
(69) Datta, S. *Quantum Transport*: Atom to Transistor; Cambridge, 2005.
(70) Nitzan, A. *J. Phys. Chem. A* **2001**, *105*, 2677–2679.
(71) Seidel, C. A. M.; Schulz, A.; Sauer, M. H. M. *J. Phys. Chem.* **1996**, *100*, 5541–5553.

a contribution that arises from the coupling of orbital m to orbital n given by the matrix elements Γ^{L}_{mn} and Γ^{R}_{nm}. These contributions can be positive or negative depending on the relative signs of the coefficients of the coupled MOs at the electrodes (coefficients of atomic orbitals coupled to the electrodes). The calculations assume that transport is coherent and that the potential drop is symmetric across the two contacts with no potential drop across the molecule. The Fermi level lies in the molecular HOMO−LUMO gap and over the range of applied bias is far enough from the MO energies so that the current−voltage curves are linear. The conductance (σ) for each structural snapshot was computed from the slope of the current−voltage curves.

Determination of Charge Transfer Rate Constants. The electron transfer between ferrocene and the electrode through the PNA is expected to be nonadiabatic. As such, the charge transfer rate is[72−82]

$$k = \frac{2\pi}{\hbar}|V|^2 \mathrm{FCWDS} \tag{5}$$

where FCWDS is the Franck−Condon weighted density of states. In the high-temperature limit

$$\mathrm{FCWDS} = \frac{1}{\sqrt{4\pi\lambda k_B T}} \exp\left[\frac{(\lambda + \Delta_r G)^2}{4\lambda k_B T}\right] \tag{6}$$

For charge transfer at an electrode, a range of electronic states in the solid is available. For a particular electrode energy, ε, the Gibbs free energy of reaction is

$$\Delta_r G = (\varepsilon_F - \varepsilon) + e\eta \tag{7}$$

where η is the overpotential and ε_F is the Fermi level energy. The rate is

$$k = \frac{2\pi}{\hbar}|V|^2 \frac{1}{\sqrt{4\pi\lambda k_B T}} \int_{-\infty}^{\infty} \rho(\varepsilon) \times \exp\left[-\frac{(\lambda + (\varepsilon_F - \varepsilon) + e\eta)^2}{4\lambda k_B T}\right] f(\varepsilon)\, d\varepsilon \tag{8}$$

where $\rho(\varepsilon)$ in the density of electronic states of the electrode and $f(\varepsilon)$ is the Fermi−Dirac distribution

$$f(\varepsilon) = \frac{1}{1 + \exp[(\varepsilon - \varepsilon_F)/k_B T}} \tag{9}$$

The standard heterogeneous rate constant k^0 corresponds to $\eta = 0$, and eq 8 becomes

$$k^0 = \frac{2\pi}{\hbar}|V|^2 \frac{1}{\sqrt{4\pi\lambda k_B T}} \int_{-\infty}^{\infty} \rho(\varepsilon) \times \exp\left[-\frac{(\lambda + (\varepsilon_F - \varepsilon))^2}{4\lambda k_B T}\right] f(\varepsilon)\, d\varepsilon \tag{10}$$

The different PNA systems should have the same reorganization energy (λ), ε_F, and $\rho(\varepsilon)$. Any differences in the charge transfer rate constant should reflect differences in the electronic coupling $|V|$ mediated by the PNA.

The connection between theory and experiment is made by comparing the calculated conductance to the experimental charge transfer rate constant. In the limit of perturbative molecule−electrode coupling, i.e., the coupling is small relative to the energy eigenvalue gaps, the conductance σ near zero bias is related to the experimental charge transfer rate k^0 by eq 11.[70]

$$\sigma \approx \frac{8e^2}{\pi^2 \Gamma^{L}_{D} \Gamma^{R}_{A} \mathrm{FCWDS}} k^0 \tag{11}$$

with FCWDS given by eq 6 and Γ^{L}_{D} and Γ^{R}_{A} are the linewidths of the donor and acceptor energy levels.

Because the conductance or charge transfer rate depends on geometries of ss-PNA strands, eq 11 cannot be applied if (a) transport is incoherent with coupling to nuclear degrees of freedom or (b) nuclear motion is slow or comparable to the charge transfer rate constant.[83,85]

Charge transport in our systems takes place in the deep tunneling regime and we estimate a Landauer−Buttiker contact time[84] for the charge with the PNA bridge to be ≤6 fs ($(\varepsilon - \varepsilon_F) \geq 0.8$ eV). The only bridge motion time scales that are comparable to 6 fs are the vibrations of bonds between hydrogen and heavy atoms, which do not influence the energies or couplings for π mediated charge transport. Thus, in this regime, transport can be assumed to be coherent. Further, the overall charge transfer rate is quite slow (several tens of milliseconds) relative to fluctuations of nucleobase geometries (from several tens of femtoseconds to picoseconds) so that the charge sees an averaged barrier for tunneling[83,85] through a single PNA strand. This limit implies that the charge transfer rate is a spatial average of rates through the ensemble of PNA strands on the SAM. Accordingly, the snapshots derived from our simulations sampled at 1 ps intervals are electronically uncorrelated and correspond to the ensemble of geometries on the SAM. Thus, eq 11 can be applied.

Results

Ellipsometry Studies. Ellipsometry was used to determine the film thickness from the change in polarization of light reflected from the SAM-coated gold surface, assuming a refractive index of 1.6.[44] Differences between the true refractive index of a PNA SAM and 1.6 will cause a systematic error in the calculated thickness value. The PNA SAM thicknesses are reported in Table 1. The lengths of the ss-PNA molecules were estimated to be 3.35 nm by adding the characteristic lengths for the cysteine (4 Å), the ferrocene (5 Å), and the PNA bases (3.5 Å per base).[86]

Table 1. Thickness of ss-PNA SAMs Determined from Ellipsometry Measurements

molecule	thickness (nm)
Cys−T3−Bk−T3−Fc	2.2 ± 0.2
Cys−T3−C−T3−Fc	2.3 ± 0.1
Cys−T3−T−T3−Fc	2.3 ± 0.1
Cys−T3−A−T3−Fc	2.5 ± 0.1
Cys−T3−G−T3−Fc	2.4 ± 0.1

The ellipsometric thicknesses for the ss-PNA SAMs were significantly less than the calculated lengths of the molecules.

(72) Barbara, P. F.; Meyer, T. J.; Ratner, M. A. *J. Phys. Chem.* **1996**, *100*, 13148–13168.
(73) Bard, A. J.; Faulkner, L. R. *Electrochemical Methods, Fundamental and Applications*: Wiley, New York, 1980.
(74) Chidsey, C. E. D. *Science* **1991**, *251*, 919–922.
(75) Finklea, H. O. In *Electroanalytical Chemistry*; Bard, A. J., Rubinstein, I., Eds.; Marcel Dekker, Inc.: New York, 1996, *19*, 109.
(76) Khoshtariya, D. E.; Dolidze, T. D.; Zusman, L. D.; Waldeck, D. H. *J. Phys. Chem. A* **2001**, *105*, 1818–1829.
(77) Marcus, R. A. *J. Chem. Phys.* **1956**, *24*, 966–978.
(78) Marcus, R. A. *J. Chem. Phys.* **1965**, *43*, 679–701.
(79) Miller, C. J. *Physical Electrochemistry: Principles, Methods and Applications*; Rubinstein, I., Ed.; Marcel Dekker, Inc.: New York, 1995; p 27.
(80) Napper, A. M.; Liu, H.; Waldeck, D. H. *J. Phys. Chem. B* **2001**, *105*, 7699–7707.
(81) Wei, J.; Liu, H.; Dick, A. R.; Yamamoto, H.; He, Y.; Waldeck, D. H. *J. Am. Chem. Soc.* **2002**, *124*, 9591–9599.
(82) Zimmt, M. B.; Waldeck, D. H. *J. Phys. Chem. A* **2003**, *107*, 3580–3597.
(83) Berlin, Y. A.; Grozema, F. C.; Siebbeles, L. D. A.; Ratner, M. A. *J. Phys. Chem. C* **2008**, *112*, 10988–11000.
(84) Nitzan, A.; Jortner, J.; Wilkie, J.; Burin, A. L.; Ratner, M. A. *J. Phys. Chem. B* **2000**, *104*, 5661–5665.

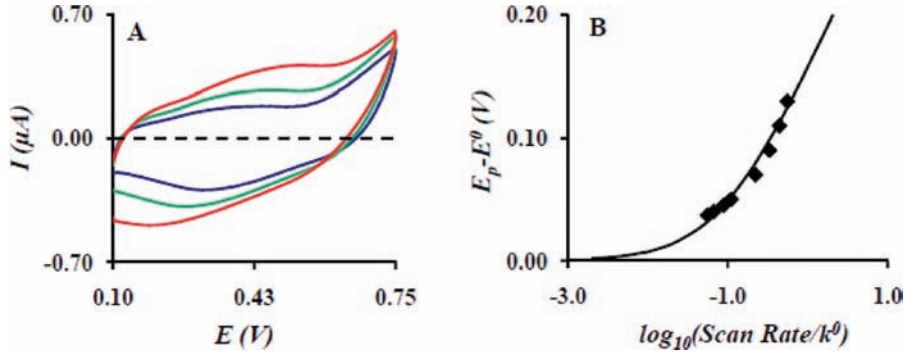

Figure 2. (A) Cyclic voltammograms are shown for Cys−T3−G−T3−Fc SAM at scan rates of 6 (blue), 10 (green), and 20 mV/s (red). (B) Fitting curves are plotted for the determination of the k^0 for Cys−T3−G−T3−Fc SAM. The black diamond symbols represent the experimentally determined points and the black solid line represents the best fit theoretical curve. E_p is the peak potential and E^0 is the apparent redox potential.

As described in our previous study,[44] this difference reflects a SAM in which a percentage of molecules are "lying-down" on the gold surface and a second population of molecules are "standing-up" on the surface (see Figure 1 schematic). A comparison of the measured SAM thickness to the 3.35 nm molecular length implies that ∼7−9% of the molecules are "lying-down" on the gold electrode.[44]

Electrochemical Characterization. For each type of ss-PNA SAM, the voltammetry indicates the presence of two different redox species. One species has a fast charge transfer rate, presumably comprised of molecules that are "lying-down" on the electrode and for which direct charge transfer from the ferrocene/ferrocenium to the gold electrode is rapid. The second species has a much slower charge transfer, and presumably is comprised of the 'standing-up' molecules for which charge transfer occurs through the PNA.[44] For each of the SAMs, the percentage of "lying-down" molecules was determined by integrating the current and found to be 8−10% of the total coverage, in good agreement with the ellipsometry measurements. The fast rate constant species, i.e., "lying-down" molecules, was made electrochemically silent by taking advantage of the fact that the "lying-down" phase preferentially reacted irreversibly with Cl^- at fast scan rates to form an electrochemically silent product.[44] Subsequently, the charge transfer rates were measured for "standing-up" molecules.

Electrochemical Results for Different PNA Molecules. The results of a voltammetry study of the Cys−T3−G−T3−Fc are shown in Figure 2. The voltammograms of other ss-PNA SAMs appear in the Supporting Information. Panel A of Figure 2 shows a representative voltammogram for Cys−T3−G−T3−Fc PNA SAMs at each of three different scan speeds. As the scan speed increases, the observed peak potential shifts because the scan speed becomes faster than the charge transfer through the PNA. These voltammetric peak shifts were fit by the predicted shift, using Marcus theory[77,78] to determine the standard heterogeneous charge transfer rate constant, k^0. Panel B shows the dependence of the oxidation peak potential as a function of the scan speed and compares it to a best fit by the Marcus model, in which k^0 was used as an adjustable parameter. The reorganization energy which is a parameter in the fit was taken as 0.8 eV.[80] Ferrocene's reorganization energy has been characterized by several research groups, and it is reported to lie between 0.7 and 0.96 eV.[47] A change of up to 25% in this reorganization energy does not change the quality of the fit. The voltammograms and fitting curves of other ss-PNA SAMs are provided in the Supporting Information.

Table 2. k^0 and Electrochemical Coverage for ss-PNA.

molecule	k^0 (s^{-1})	coverage (pmol/cm^2)	no. of trials
Cys−T3−Bk−T3−Fc	<0.005	∼100	5
Cys−T3−C−T3−Fc	0.014 ± 0.003	91 ± 28	6
Cys−T3−T−T3−Fc	0.018 ± 0.002	83 ± 13	4
Cys−T3−A−T3−Fc	0.041 ± 0.010	96 ± 28	4
Cys−T3−G−T3−Fc	0.076 ± 0.013	87 ± 26	5

Table 3. Computed Conductance (σ) for the Four T3−X−T3 Systems

molecule	mean σ, <σ> (10^{-12} Ω^{-1})	median σ, $\tilde{\sigma}$ (10^{-12} Ω^{-1})	max σ (10^{-10} Ω^{-1})
Cys−T3−C−T3−Fc	0.77	0.30	0.11
Cys−T3−T−T3−Fc	0.42	0.28	0.04
Cys−T3−A−T3−Fc	4.25	1.66	0.59
Cys−T3−G−T3−Fc	5.91	3.08	1.10

Charge transfer rate constants for the five different ss-PNAs are reported in Table 2. The CT rate constant of Cys−T3−C−T3−Fc was comparable to that of Cys−T7−Fc. The charge transfer rate constant of Cys−T3−G−T3−Fc and Cys−T3−A−T3−Fc are four times and two times faster, respectively, than that of Cys−T7−Fc. The rate constant for Cys−T3−Bk−T3−Fc was more than three times slower than that of Cys−T7−Fc. Comparison of Cys−T3−G−T3−Fc and Cys−T3−Bk−T3−Fc reveals a more than 15-fold difference in k^0.

We investigated the role of interchain coupling in the ss-PNA SAMs, i.e., charge transfer involving different PNA strands, by studying two different mixed ss-PNA SAM films, Cys−T7/ Cys−T7−Fc and Cys−T3−G−T3/ Cys−T7−Fc. In each case, the PNA strands that had a ferrocene reporter constituted 50% of the SAM, and the remainder was a diluent PNA without ferrocene. If the charge transfer involves significant tunneling or hopping via nucleobases situated on neighboring strands, then the presence of a G base in the diluent PNA should cause a significant enhancement of the rate constant. The observed rate constants for the SAM with the G base in the diluent showed only a 10% increase over that for the film containing only T nucleobases, a difference that is within the experimental error. Therefore, we conclude on the basis of this experiment that the charge transport is mediated primarily by individual strands.

(85) Bixon, M.; Jortner, J. *Russ. J. Electrochem* **2003**, *39*, 3.
(86) The length of Cysteine, Ferrocene, and each PNA base has been calculated by CAChe software. Geometry has been optimized by PM3 method.

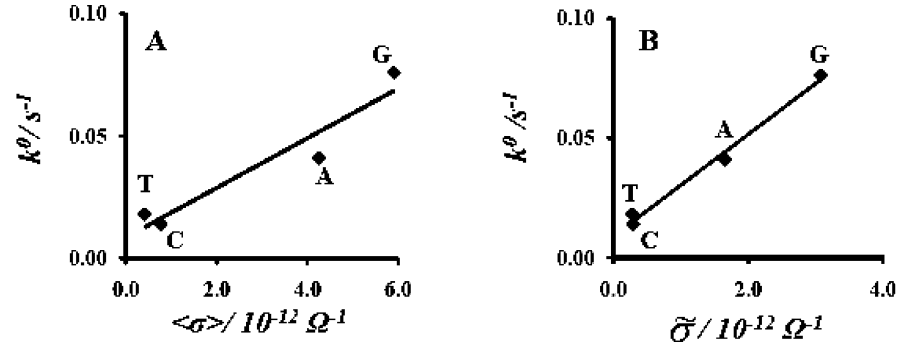

Figure 3. Experimental charge transfer rate constant plotted versus the calculated conductances (the average conductance in panel A and the median conductance in panel B). Each plot has four data points corresponding to the four ss-PNA systems T3−X−T3. Linear best fits for each data set are shown.

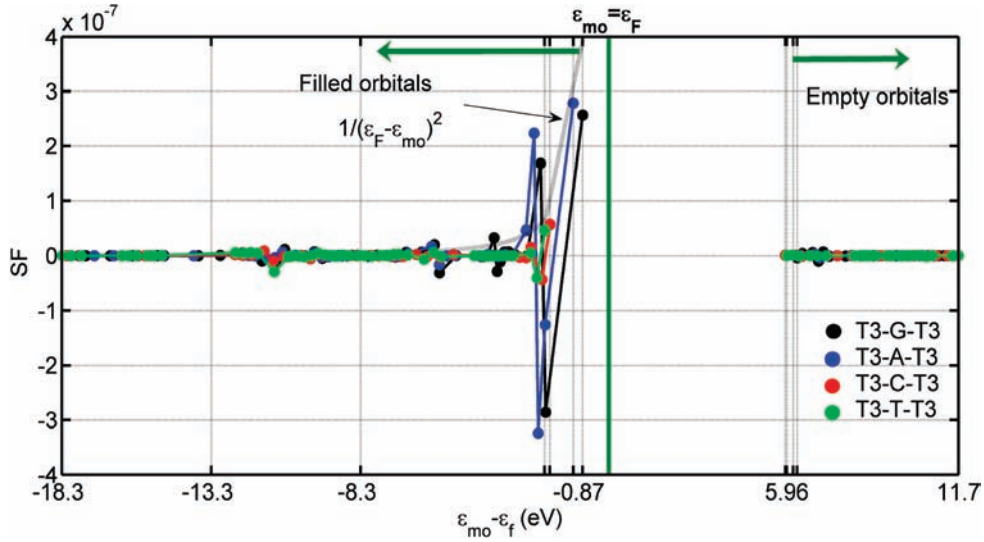

Figure 4. Plots of average dimensionless scoring factor (eq 4) for each molecular orbital versus the energy difference: $\varepsilon_{mo}-\varepsilon_F$, where ε_{mo} is the molecular orbital energy and ε_F is the Fermi energy. The gray line shows the functional form of the denominator term in eq 4 (for $i = j$).

Computational Results. Table 3 shows the mean, median and maximum conductance values calculated for the MD structures of T3−X−T3 system. In agreement with the experimental trends, the purine-containing PNAs (X = G, A) show much higher conductance than the pyrimidine-containing PNAs (X = C, T). The computed conductance for a set of 500 structures has a skewed distribution, with the maximum conductance about one to two orders of magnitude larger and the minimum conductance about one to two orders of magnitude lower than the average value (see Figure S10 in the Supporting Information). As discussed previously, the distributions may be skewed because of the initial structure used in the MD simulations (cf. Figure 7 below).

If the coupling of the molecule to the electrode and the ferrocene is small enough, a linear relationship is expected[70] between the conductance near zero bias and the charge transfer rate (eq 11). Figure 3 shows a plot of k^0 versus the mean conductance $\langle\sigma\rangle$ in panel A and k^0 versus the median conductance $\tilde{\sigma}$ in panel B for each of the four PNAs. The calculated conductance correlates well with the experimental rate constants. The coupling elements of the broadening matrix were estimated by using the slope from the plot in Figure 3A with eq 11. The FCWDS was evaluated by using eq 6 with a reorganization energy of 0.8 eV[44,80] and $\Delta_r G = 0$. Assuming that the coupling to electrodes induces equal linewidths on the donor and acceptor, we obtain $\Gamma_D^L = \Gamma_A^R = 0.133$ eV for the linewidths in eq 11.

Figure 4 shows the average contributions (for the 500 MD structures) of filled and empty MOs to the conductance in terms of the scoring factor defined by eq 4. For all four T3−X−T3 systems, the sum of contributions from filled orbitals exceeds that from empty orbitals by two orders of magnitude, which indicates that hole-mediated superexchange (or hole transfer) dominates the electronic coupling. For all four PNAs, the highest filled orbitals give the largest contribution to hole transfer and the scoring factor falls off rapidly as the energies of the orbitals shift away from ε_F. Because the total conductance (or current) is proportional to the sum of contributions from all orbitals, it is of interest to determine the dominant orbital contributions for the four systems. The top 3 (T3−G−T3), 5 (T3−A−T3), 38 (T3−C−T3), and 42 (T3−T−T3) filled orbitals are required for the sum to converge to 80% of the total contribution from all filled and empty orbitals (see Figure S8 in the Supporting Information).

The stark difference in the number of orbitals that make a major contribution to the conductance for purines vs pyrimidines may be rationalized by using energetic arguments. The energy difference between ε_F and the HOMO is ∼1 eV larger for the pyrimidine-containing PNAs than for the purine-containing PNAs. This difference results in a smaller scoring factor for the pyrimidine frontier orbitals than for the purine orbitals. Because the contacts between the TXT core and the rest of the PNA oligomers induce a coupling between orbitals, the scaling

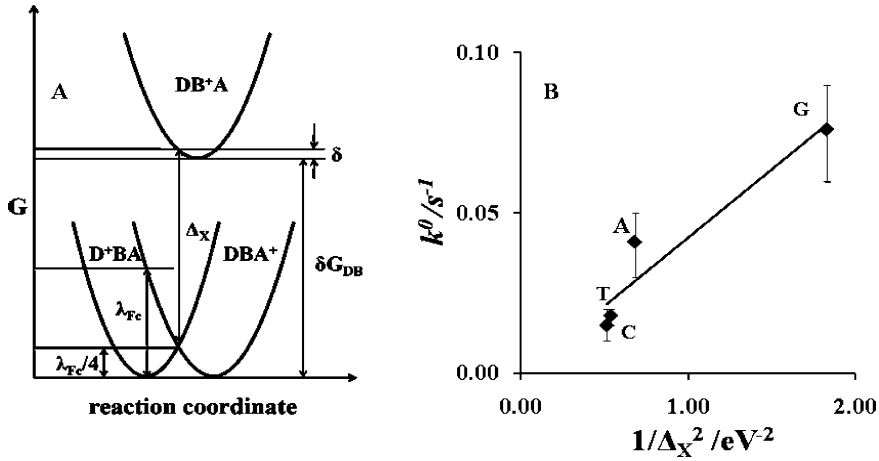

Figure 5. (A) Energetic considerations for calculating the tunneling barrier; in this case D is the electrode, B is the PNA bridge, and A is the ferrocene. (B) k^0 values of the different ss-PNA SAMs are plotted versus $(1/\Delta_X)^2$. Black diamond symbols represent experimentally determined points for ss-PNA SAMs and the black straight line is the best fit straight line between the experimentally determined results.

of the HOMO energy affects other filled orbitals coupled to the HOMO (Figure 4). For the purine-containing PNAs, the contributions from these few highest filled coupled orbitals is large enough to dominate the total contribution from all orbitals. However, for the pyrimidine-containing systems, the contribution of the highest filled orbitals is scaled down and the relative contribution of the lower lying orbitals is larger.

Although the number of orbitals contributing to the total current changes with PNA sequence, the contribution from the energetically low-lying orbitals is similar in all four PNAs (see Figure S9 in the Supporting Information). The difference in conductance (or current) among the four PNAs arises from differences in the contributions from the highest filled orbitals, i.e., the HOMO and the orbitals strongly coupled to it, that have very different energies in each of the four PNAs. For all four PNAs, the strongly contributing HOMO, HOMO-1, and HOMO-2 have π character and are strongly localized on one of the three TXT nucleobases of the core, indicating that the electronic coupling among the nucleobases is small compared to the energy difference among nucleobase orbitals.

Discussion

For the ss-PNA SAMs, the k^0 values ranged from 0.014 to 0.067 s^{-1}, indicating that the nucleobases play an important role in determining the charge transfer rate through the ss-PNA SAMs. The very slow charge transfer rate constant found for Cys−T3−Bk−T3−Fc (<0.005 s^{-1}) further confirms the role played by the nucleobases.

The computational studies indicate that the four T3−X−T3 systems have weak nearest neighbor electronic couplings, and that MOs localized on individual nucleobases dominate the coupling. These conclusions validate the use of a McConnell-like coupling model[87] to describe differences in charge transfer rates among the T3−X−T3 PNA oligomers. For a donor (D) and acceptor (A) with a chain of identical bridge states (B), the model gives

$$|V| = \left(\frac{h_{DB}h_{BA}}{\Delta}\right)\left(\frac{h}{\Delta}\right)^{N-1} \tag{12}$$

where h_{DB} (h_{BA}) is the electronic coupling between the donor (acceptor) and the terminal unit of the bridge. Δ represents the energy gap between the Fermi level and the mediating orbitals of the bridge, and it is approximated as the energy to place an electron (or hole) from the crossing point of donor−acceptor Marcus parabolas (see Figure 5A) onto a bridge unit without nuclear relaxation (a "vertical" energy). This energy can be estimated using the redox potential of the nucleobase and the reorganization energies of the intervening nucleobases and the acceptor. h is the electronic coupling between the adjacent bridge sites. For a single variable site in the center of the bridge

$$|V| = \left(\frac{h_{FcT}h_{TAu}}{\Delta_T^2}\right)\left(\frac{h_{TT}}{\Delta_T}\right)^4\left(\frac{h_{TX}h_{XT}}{\Delta_X}\right) \tag{13}$$

where h_{TAu} is the gold−thymine coupling (including the cysteine) and h_{FcT} is the thymine−ferrocene coupling, respectively. The thymine−thymine (T−T) coupling is h_{TT}, the coupling between T and the unique base is h_{TX}, and the vertical tunneling energy gaps are Δ_T and Δ_X. Because only one base was varied in this study, we postulate that the relative charge transfer rates are proportional to h_{TX}, h_{XT}, and Δ_X.

Assuming further that h_{TX} and h_{XT} do not vary significantly (on average) with X (for X = G, A, T, C), rate differences result from Δ_X. Because $|V_X|$ is proportional to $1/\Delta_X$, the rate constant is proportional to $(1/\Delta_X)^2$, and a plot of k^0 versus $(1/\Delta_X)^2$ should be linear. Because the simulations suggest that charge transfer is hole mediated, we use the oxidation potential of the nucleobase X, $E_{ox}(X)$, to estimate the tunneling barrier. Δ_X is the vertical energy difference between the crossing point for the ferrocene/ferrocenium Marcus parabolas and the oxidized bridge parabola; hence

$$\Delta_X = E_{ox}(X) - E_{ox}(Fc) - \frac{\lambda_{Fc}}{4} + \delta \tag{14}$$

where $E_{ox}(Fc)$ is the ferrocene redox potential (0.45 V vs Ag/AgCl) and λ_{Fc} is the ferrocene reorganization energy (0.8 eV). The nucleobase oxidation potentials are taken from the report of Seidel et al.[71,88] to be $E_{ox}(G) = 1.25$ V, $E_{ox}(A) = 1.72$ V, $E_{ox}(T) = 1.87$ V, and $E_{ox}(C) = 1.90$ V vs Ag/AgCl. The parameter δ accounts for the energy shift that arises from any displacement of the nucleobase's Marcus parabola away from the crossing point of the donor−acceptor curves for the ferrocene/ferrocenium reaction (see Figure 5A). Figure 5B plots the charge transfer rate constant versus $(1/\Delta_X)^2$ for the different systems; note that the fit is restricted to go through the origin

(87) McConnell, H. M. *J. Chem. Phys.* **1961**, *35*, 508–515.

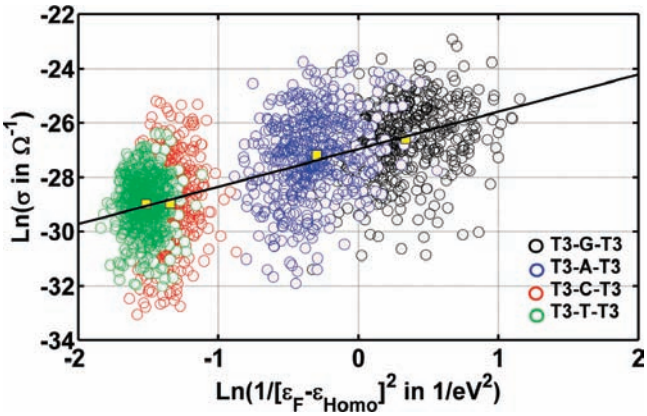

Figure 6. Scatter plot showing strong correlation (a linear fit) between the average energy gap and $\langle\sigma\rangle$ and a weak correlation between the energy gap and σ for each T3−X−T3 system.

(i.e., zero coupling as $\Delta \rightarrow \infty$). The charge transfer rate constant decreases as the energy difference between the central nucleobase and the tunneling energy increases, consistent with a superexchange mechanism. The parameter δ is estimated to lie between 0 and 0.26 eV after accounting for errors in the experimentally measured rates ($\delta = 0.14$ eV for the fit in figure 5B)[89] and suggests that the minima for the bridging nucleobase Marcus parabolas lie near the crossing point of donor−acceptor parabolas.

The limitation of the McConnell model, as well as the importance of variations in the interbase electronic coupling, is evident from the analysis of calculated conductance and electronic structure for the geometries sampled from MD simulations. Figure 6 plots the conductance values σ and the ensemble averaged conductance $\langle\sigma\rangle$ versus the average energy gap denominator in eq 4 ($<D_{SF}> = <1/(\varepsilon_F - \varepsilon_{m=HOMO})^2>$) for each of the T3XT3 systems. The plot shows a strong correlation between $\langle\sigma\rangle$ and $<D_{SF}>$; the linear fit is shown in the figure and has a correlation coefficient of 0.95. This correlation indicates that the average couplings among MOs (localized on the nucleobases) are quite similar for all of the bases X = G, A, C, T, as assumed in the simple McConnell description. In the limit of Koopmans' theorem, the HOMO energy corresponds to the oxidation potential of the base X, and explains the simple linear dependence of Figure 5. Although the averaged conductance correlates well with the energy gap, the scatter in the conductance values makes it clear that a large range of conductances may occur for different molecular conformations within a narrow range of energy gaps. The last column in Table 4 reports the weak correlation between calculated conductance and D_{SF} for each T3XT3 system. In the set of 500 structures, the nearest neighbor couplings vary considerably for each T3XT3 system, and σ is modulated more strongly by nearest neighbor coupling fluctuations than by orbital energy fluctuations. Thus, while the McConnell model appears to provide a reasonable description for the variation in the average conductance with the average energy gap of the nucleobase X across the four T3XT3 systems, it must be interpreted within an ensemble averaged framework to describe the observed trend in rates.

Table 4. Comparison of the Calculated Conductance (σ) with the Energy Gap (the Denominator Term in eq 4 for $n = m =$ HOMO)

molecule	ε_{HOMO} in eV	$<D_{SF}> = <1/(\varepsilon_F-\varepsilon_{HOMO})^2>$ in 1/eV^2	$<\ln(\sigma)>$ σ in Ω^{-1}	correlation coefficient
T3−G−T3	−7.57 ± 0.13	1.40 ± 0.43	−26.61 ± 1.33	0.19
T3−A−T3	−7.88 ± 0.14	0.74 ± 0.19	−27.19 ± 1.54	0.24
T3−C−T3	−8.67 ± 0.11	0.26 ± 0.03	−28.97 ± 1.56	0.07
T3−T−T3	−8.84 ± 0.12	0.22 ± 0.02	−28.98 ± 1.04	0.05

The dependence of conduction on the interactions among the nucleobases is further revealed by an analysis of the MD geometries that generate the maximum, minimum, and average conductance values. For each T3−X−T3 PNA, the structural snapshots with minimum conductance displayed structural deformations that affected the π-stacking of the central base with one of the neighboring T bases (see Figure 7). The conductance depends on two geometric parameters: (1) the aromatic ring overlaps, defined as the area of one ring projected onto the plane of the other, and (2) the minimum distance between the adjacent nucleobases. To quantify the dependence of conductance on these two parameters, we calculated the conductance as a function of the nucleobase step helicoidal parameters: shift, slide, rise, roll, tilt, and twist. Modification of each of the parameters affected the distance between adjacent nucleobases and their aromatic ring overlap, resulting, in some cases, in dramatic changes in the conductance (see Figure S3 in the Supporting Information). The structural differences between maximum and minimum conductance geometries are greatest for T3−A−T3 and T3−C−T3, with the former showing more variation of the aromatic ring geometric overlap and the latter showing more variation in interbase distance. The differ-

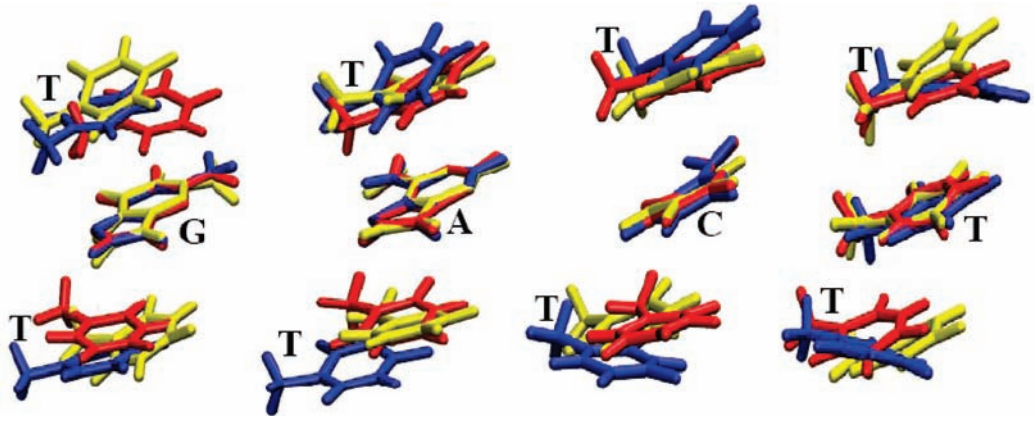

Figure 7. T3−X−T3 structures showing maximum (red), minimum (blue), and average (yellow) conductance values; the structures are taken from an ensemble of 500 structures generated by molecular dynamics.

ences between maximum and minimum conductance geometries are lowest for the all T-oligomers.

Conclusions

In this study, 7-mer ss-PNAs with the sequence T3−X−T3 were self-assembled on a gold electrode. The charge transfer rate constants for these SAMs depend on the nucleobase X. Consistent with earlier studies of DNA/PNA, both experiment and theory indicate that the charge transfer rate constant and the average conductance, respectively, decreases in the order T3−G−T3 > T3−A−T3 > T3−C−T3 ≈ T3−T−T3. The theoretical conductance values show a strong linear correlation with the experimental charge transfer rate constants. The strong correlation between the trends in the experimental rate constants and in the calculated conductances based on MD simulations of single ss-PNA molecules supports the conclusions from mixed ss-PNA monolayers that charge transport is mediated primarily by individual strands.

Computational studies show that charge transfer through the PNA SAMs occurs by hole-mediated superexchange. This conclusion is supported by the observed correlation between the charge transfer rate constant and the oxidation potential of the central base X in the T3−X−T3 PNAs. Computations show that, while the charge transfer rate is dependent on both electronic energies and couplings between nucleobases, similar stacking geometries of the four T3−X−T3 systems produce similar nearest neighbor electronic couplings (on average). Furthermore, the weakness of the couplings produces MOs that are localized on individual nucleobases. The charge transfer rate constant is thus modulated primarily by the oxidation potential of the nucleobase X.

It is important to distinguish the current finding from earlier reports that the stacked DNA bases form a conduit for ultrafast radical cation migration.[11,90,91] Studies of radical migration display a weak dependence on length (number of nucleobases). In contrast, the present studies are carried out in the large barrier regime and produce rapid exponential decay of rate with increasing number of nucleobases.[44]

Acknowledgment. D.H.W., D.N.B., and C.A. acknowledge support from the National Science Foundation (CHE 0628169). A.P. thanks Dr. Andrew M. Napper and Dr. Jianjun Wei for useful discussions during this study. C.A. acknowledges support by the Sloan Foundation and the Camille and Henry Dreyfus Foundation. We thank Prof. Jeffrey R. Reimers for the CNDO computer code. We also thank Kathryn L. Davis and Dr. Richard M. Watson for useful discussions.

Supporting Information Available: Plots showing the variation of conductance with nucleobase-step helicoidal parameters, cyclic voltammograms, fitting curves of charge transfer rate constants, MALDI-ToF mass spectrometry data for PNA molecules, and plots showing the sum of scoring factors for different molecular orbitals. This material is available free of charge via the Internet at http://pubs.acs.org.

JA9000163

(88) Boussicult and Robert[89] report values of nucleobase oxidation potentials which differ significantly from those reported by Seidel et al. Using the values reported by the former we obtain a much better fit for the plot in figure 5B. Here the values of δ are estimated to be significantly higher in the range between 0.31 and 0.68 eV.

(89) Boussicault, F.; Robert, M. *Chem. Rev.* **2008**, *108*, 2622–2645.

(90) Gorodetsky, A. A.; Buzzeo, M. C.; Barton, J. K. *Bioconjugate Chem.* **2008**, *19*, 2285–2296.

(91) O'Neill, M. A.; Barton, J. K. *J. Am. Chem. Soc.* **2004**, *126*, 11471–11483.